ISSN: 2230-9926

Available online at http://www.journalijdr.com

IJDR

International Journal of Development Research
Vol. 09, Issue, 11, pp. 31435-31442, November, 2019

RESEARCH ARTICLE OPEN ACCESS

EFFECT OF THE ANNEALING TEMPERATURE ON PHASE COMPOSITION OF IRON OXIDE NANOPARTICLES

[1]Renilma S. P. Fonseca, *[2]Francisco S. M. Sinfrônio, [2]Inocêncio S. S. Neto, [1]Mikaelly D. F. Borges, [1]Fernando C. Silva, [3]Alan S. Menezes, [3]Surender K. Sharma and [4]Andris F. Bakuzis

[1]Department of Chemistry, Federal University of Maranhão, Campus of Bacanga, São Luís, 65080-805, Brazil
[2]Department of Electrical Engineering, Federal University of Maranhão, Campus of Bacanga, São Luís, 65080-805, Brazil
[3]Department of Physics, Federal University of Maranhão, Campus of Bacanga, São Luís, 65080-805, Brazil
[4]Institute of Physics, Federal University of Goiás, Campus of Samambaia, Goiânia, 74690-900, Brazil

ARTICLE INFO

Article History:
Received 18th August, 2019
Received in revised form
03rd September, 2019
Accepted 13th October, 2019
Published online 30th November, 2019

Key Words:
Iron oxide nanoparticles;
Thermal decomposition method;
Phase transition.

Corresponding author:
Francisco S. M. Sinfrônio

ABSTRACT

In this study, we investigated the effect of the annealing temperature on the phases and magnetic properties of iron oxide. Iron oxide nanoparticles were obtained by the thermal decomposition reaction method at different oxidation temperatures (125, 150, 200, and 250 °C). The X-ray powder diffraction data indicate the formation of three different iron oxide phases, being controlled by the annealing temperature: Fe_3O_4 » (Fe_3O_4 +α-Fe_2O_3) » (Fe_3O_4+ α-Fe_2O_3+β-Fe_2O_3). The infrared data confirmed the formation of iron oxide phases in the iron oxide nanoparticles as well as the functionalization of their surfaces by both oleylamine and oleic acid molecules. ZFC-FC analysis suggests the all nanoparticles particles obtained under 250 °C are in the blocked regime. At 300 K, the superparamagnetic contribution for the iron oxide nanoparticles was proportional to the annealing temperature.

Citation: Renilma S. P. Fonseca, Francisco S. M. Sinfrônio, Inocêncio S. S. Neto, Mikaelly D. F. Borges *et al.* 2019. "Effect of the annealing temperature on phase composition of iron oxide nanoparticles", *International Journal of Development Research*, 09, (11), 31435-31442.

INTRODUCTION

Over the past few years, superparamagnetic iron oxide nanoparticles have gained extensive attention as contrast agents for magnetic resonance imaging, as chemical media for drug delivery processes, and in hyperthermia technique (novel alternative cancer treatment) owing to their unique size-dependent physicochemical and magnetic properties (Soares, 2012; Abenojar, 2016; Anjum, 2017; Nigam, 2017). Hence, several studies have been carried out to control the polymorphic transition mechanism of such materials in order to improve their physicochemical characteristics and biocompatibility. The polymorphism of iron oxide nanoparticles can be attributed to their ability to exist in multiple anhydrous and hydrous forms that ensure their stability over a wide range of environmental conditions. The formation of hydroxides, oxide-hydroxides, and oxides during mineralization strongly depends on the level of oxidation, iron concentration, type and activity of counter ions, and pH of the reactant solution (Wu, 2016). Small perturbations in the reaction conditions can change the phase of the obtained iron oxides. Under extreme reducing conditions, iron oxides with a non-stoichiometric rock salt structure (wüstite- FeO) are obtained. On the other hand, under oxidizing conditions, α–Fe_2O_3 (i.e., hematite), β-Fe_2O_3, ε-Fe_2O_3, and γ-Fe_2O_3 (i.e., maghemite) with unique magnetic properties are formed (Tuček, 2015; Machala, 2011; Brázda, 2014). Hematite (α–Fe_2O_3) has a rhombohedral lattice structure (space group $R\bar{3}c$) and is the most stable iron oxide (Wu, 2016). Its magnetic behavior depends on its average particle size. The Néel temperature (T_N) of hematite is approximately 960 K, whereas its Morin transition temperature (T_M) is about 263 K. Hence, this phase exhibits ferromagnetism at temperatures higher than T_M and antiferromagnetism at temperatures lower than T_M (Kamali, 2013). In this case, a decrease in the particle size

results in a reduction of both T_N and T_M, which generates very small lattices. Furthermore, iron oxide nanostructures (particle size = <10 nm) show superparamagnetism at temperatures higher than the blocking temperature (T_B) and ferromagnetism at temperatures lower than T_B (Tadic, 2014). At ambient temperature, α–Fe_2O_3 behaves as an n-type semiconductor material, which makes it suitable for photoelectrochemical processes (Meng, 2016; Tamirat, 2016). The metastable phase, β- Fe_2O_3, crystallizes below 770 K (Danno, 2013). It has a body-centered cubic "bixbyite" structure (space group of $Ia\bar{3}$) (Malina, 2014; Emery, Emery). This type of structure consists of 32 ions in a state of high rotation arranged in two crystallographic non-equivalent octahedral sublattices. Among these ions, 24 Fe^{3+} ions occupy the *d-sites* with the C_2 symmetry and the remaining 8 Fe^{3+} ions occupy the *b-sites* with the C_{3i} symmetry (Zboril, 2004). This is the only iron polymorph showing paramagnetic behavior at room temperature and antiferromagnetic ordering below the Néel temperature (Malina, 2015).

Conversely, ε-Fe_2O_3 is a rare metastable iron polymorph, which stabilizes in the form of nanoparticles and is hardly generated as a single phase. The epsilon phase has an orthorhombic structure (space group $Pna2_1$) and is generated by processes with a high control of the particle size and coalescence (Kohout, 2015; Xu, 2018). This structure shows a high gigahertz frequency absorption and extremely large coercive field (~20 KOe) because of its strong spin-orbit coupling (Yakushkin, 2018; Maccato, 2018). Moreover, it is a co-linear ferrimagnetic material undergoing Curie transition (~510 K) (Sánchez, 2017). Maghemite, γ-Fe_2O_3, is the second most abundant iron polymorph (second only to α-Fe_2O_3) found in the earth's crust (Ma, 2018). Its inverse spinel-type crystalline structure is similar to that of magnetite. This structure is often reported either as a cubic structure (space group P4332) with a partial Fe vacancy disorder or as a tetragonal structure (space group P41212) with full site ordering (Fock, 2017). Since magnetite is deficient in Fe^{3+} cations, it shows cationic vacancies in the octahedral sublattices, which affect the unit cell parameters Development of a biocompatible magnetic nanofluid by incorporating SPIONs in Amazonian oils (Gaspar, 2017). Unfortunately, γ-Fe_2O_3 transforms into α–Fe_2O_3 at a rather low temperature (~300 °C). Its biocompatible nature (low toxicity), oxidation stability, and good ferrimagnetic properties (usually shows superparamagnetism when obtained in the form of nanoparticles) make it suitable for various applications Maghemite, γ-Fe_2O_3, nanoparticles preparation via carbon-templated solution combustion synthesis (Ianoş, 2018). Magnetite, Fe_3O_4, has an inverse-type spinel crystalline structure with the centered cubic unit cell configuration and the spatial group of $Fd\bar{3}m$(Williams, 2018). In this structure, the octahedral sublattices are occupied by ferrous cations (Fe^{2+}) and half of the ferric cations (Fe^{3+}), whereas the tetrahedral sublattices are occupied by the other half of the ferric ions(Jin, 2018).

The preparation mode and particle size play an important role in determining the ease of formation of such polymorph structures. For instance, hematite is crystallized under oxidizing conditions, while magnetite (inverse spinel) is generated under moderate environments. Fe_3O_4 is formed under highly oxidative conditions by the vigorous conversion of Fe^{2+} to Fe^{3+} and the compensation of iron vacancies in the octahedral sublattices of the spinel crystal.

In fact, controlling the chemical composition and structure of iron oxides is a great industrial challenge since they are critical parameters governing their physicochemical and magnetic properties, especially at the nanometer scale. In this study, we investigated the effect of the oxidation temperature on the phase distribution of iron oxides prepared via the thermal decomposition method.

Experimental

Synthesis of iron oxide nanoparticles: Iron (III) chloride hexahydrate ($FeCl_3$. $6H_2O$, 90%, Synth), 1-octadecene ($C_{18}H_{36}$, 90%, Sigma Aldrich), oleylamine (OL, $C_{18}H_{37}N$, 70%, Sigma Aldrich), oleic acid (OA, $C_{18}H_{34}O_2$, PA, Synth), ethanol (C_2H_6O, 99.5%, Quimex), and toluene (C_7H_8, 99.5%, Quimex) were of the analytical grade and were used without further purification. Iron oxide nanoparticles were synthesized via the thermal decomposition method (Sarveena, 2016) using iron (III) chloride hexahydrate as the metallic precursor, 1-octadecene as the solvent, OL as the reducing agent, and OA as the surfactant. In a typical procedure, 2.0 mmol of $FeCl_3.6H_2O$ was dissolved in 20.0 mL 1-octadecene, 8.0 mL OA, and 12.0 mL OL. This solution was gently heated at 120 °C for 60 min under N_2 atmosphere (100 mL.min^{-1}) and continuous stirring (600 rpm). Then, the reaction temperature was increased to 300 °C and the mixture was stirred for another 60 min. The reaction mixture was then cooled down to different annealing temperatures (125, 150, 200, and 250 °C) under synthetic air atmosphere (30 min). The final solution was then cooled to room temperature and the obtained nanoparticles were washed by adding ethanol and centrifuging at 3600 rpm (15 min). This procedure was repeated four times by dispersing the as-synthesized nanoparticles in toluene and ethanol followed by centrifugation. Finally, the nanoparticles were dispersed in 10 mL of toluene (mixed with three drops of oleylamine) for long-term storage.

Characterization

X-ray powder diffraction (XRPD) measurements were carried out using a D8 Advance diffractometer (Bruker) with a Cu K_α (λ=1.5406 Å) tube operating at 40 kV/40 mA and a LynxEye linear detector. The data were collected in the Bragg-Brentano geometry over the 2θ range of 20–100° with a step size of 0.02° and counting time of 0.5 s. The XRPD peaks of the samples were indexed using the Joint Committee Powder Diffraction Standards (JCPDS) data for phase evaluation. The XRPD patterns of the samples were analyzed using the Rietveld method. The crystallite sizes (D) of the samples were estimated using the William–Hall equation (Eq. 1):

$$B\cos\theta = k\lambda/D + 4\varepsilon\sin\theta \quad (1)$$

where B is the full width at half of maximum (in radian) of the peaks, θ is the peak position, k is the Scherrer constant (0.89), λ is the X-ray wavelength, D is the crystallite diameter, and ε is the lattice strain of the structure.

Fourier transform-infrared spectroscopy (FTIR) was carried out using an IR prestige-21 infrared spectrometer (Shimadzu) using KBr as the dispersant agent (1:100 wt./wt.). The FTIR spectra were recorded over the wavenumber range of 400–1000 cm^{-1}. The magnetization vs. temperature curves of the samples were obtained via ZFC-FC (zero-field-cooling, field-cooling) in order to investigate their super paramagnetic

behavior. Thus, the samples were cooled from 300 K to 5 K in the absence of the magnetic field. At 5 K, a static magnetic field of H = 50 Oe was applied to the samples and their ZFC was measured during heating to 300 K. The samples were then cooled to 5 K in the presence of the same magnetic field (H = 50 Oe) and their FC was measured during cooling.

RESULTS AND DISCUSSION

Structural Properties

Figures 1(a) and 1(b) show the XRPD patterns and Rietveld refinement of the iron oxide nanoparticles and their phase content distribution as a function of the oxidation temperature, respectively. All the diffraction peaks were indexed according to the JCPDS database. Three iron oxide polymorphs (magnetite, hematite, and the metastable phase, β-Fe_2O_3) were generated during the oxidation processes. Magnetite (Fe_3O_4 - ICSD 65340) with the spinel structure and space group of $Fd\bar{3}m$, showed XRPD peaks at 2θ = 30.11°, 35.51°, 43.18°, 53.52°, and 62.50° corresponding to the (022), (311), (004), (422), and (044) crystal planes, respectively. Hematite (α-Fe_2O_3 - ICSD 81248) with the rhombohedral structure and space group of R-3cH showed peaks at 2θ = 24.09°, 33.12°, 35.62°, 40,85°, 49.43°, 54.98°, 62.44°, and 64.04° corresponding to the (012), (104), (110), (113), (024), (116), (214), and (030) crystal planes, respectively. The metastable phase, β-Fe_2O_3, (ICSD 237290) with the cubic structure and space group of Ia3 showed peaks at 2θ= 23.12°, 38.21°, 40.73°, 55.11°, and 65.80° corresponding to the (211), (004), (411), (044), and (622) crystal planes, respectively. From the XRPD patterns, it can be observed that all the polymorphs crystallized as nanoparticles independently of the applied annealing temperature (Table 1).

Iron oxide polymorphism can be associated with the amount of oxygen purged into the system during the annealing process. An oxidative atmosphere gives rise to various structural disorders in the crystal lattice due to oxygen vacancies, which alter the free energy of crystallization. In thermodynamic terms, crystallization is a complex mechanism in which several metastable structures assemble until a final stable phase, Fe_3O_4, is obtained as a consequence of the gradual reduction in the Gibbs energy (Navrotsky, 2004). Hence, it can be stated that the iron oxide conformation is coordinated by the system proposed by Ostwald. Table 1 shows that the transformation of the crystalline structures of iron oxide as function of the annealing temperature occurred in the order: Fe_3O_4» (Fe_3O_4 +α-Fe_2O_3) » (Fe_3O_4+ α-Fe_2O_3+β-Fe_2O_3). In bulk, the transformation of Fe3O4 to α-Fe2O3occurs due to oxidation ($4Fe_3O_4 + O_2 \rightarrow 6Fe_2O_3$) and/or redox-reactions ($3Fe_3O_4 \rightarrow 4Fe_2O_3 + Fe$). However, the changes in the crystalline structure of nanometric systems is related to the superficial enthalpy and activation energy even at room temperature (Vasylkiv, 2016). In oxidative media, the β-Fe_2O_3 phase transforms to the α-Fe_2O_3 phase (Machala, 2011).

Vibrational Properties

Oleylamineand oleic acid are used in the synthesis of iron oxide nanoparticles because they can prevent the agglomeration of particles during the growth stage (Harris, 2015). In this study, the functionalization of the iron oxide surfaces by chemisorption of organic ligands on them was examined by FTIR spectroscopy. The iron oxide surfaces showed vibrational modes below and above 800 cm^{-1}. The peaks observed below 800 cm^{-1} corresponded to the Fe_3O_4 particles, whereas those observed above 800 cm^{-1} correspond to the OA and OL absorption on the solid surfaces (Fig. 2) (Vuong, 2015). The peaks at 2920 and 2850 cm^{-1} can be attributed to C-H stretching (Lobato, 2017). The peaks at 1500 and 1458 cm^{-1} correspond to the asymmetric and symmetric stretching vibrations of the carboxyl group of oleylamine, respectively (Darwish, 2017). Moreover, the wavenumber difference of these two peaks (Δ = 48 cm^{-1}) suggests that a bidentate chelating ligand was chemisorbed as a self-assembled monolayer (Mondini, 2013). The peaks observed in the wavenumber range of 1378–1610 cm^{-1} correspond to the NH_2 groups of oleylamine (Xu, 2018). Finally, the vibrational modes at about 550 and 441 cm^{-1} can be attributed to the Fe^{2+} ions at the tetrahedral and octahedral sublattices of the spinel ferrites, respectively (Aliramaji, 201).

Table 1. Phase distribution, lattice parameter, and average crystalline size of the iron oxide nanoparticles as function of the oxidation temperature

Annealing temperature (°C)	Phase structure	Phase content (%)	a (Å)	D (nm)	Gof	R_w
125	Fe_3O_4	100.00	8.32	1.16	1.08	3.42
	Fe_3O_4	83.13	8.38	1.81	1.10	3.82
150	α- Fe_2O_3	16.87	5.03	9.76		
200	Fe_3O_4	47.09	8.40	1.47		4.94
	α- Fe_2O_3	39.51	5.03	82.50	1.20	
	β- Fe_2O_3	13.39	9.41	91.81		
250	Fe_3O_4	63.37	8.38	4.91	1.22	6.10
	α- Fe_2O_3	31.60	5.04	1.36		
	β- Fe_2O_3	5.03	9.40	71.02		

Table 2. Saturation magnetization, magnetic remanence, and coercivity of the oxidized nanoparticles at 125, 150, 200, and 250 °C

Annealing temperature (°C)	M_s (emu)		M_r (emu)		-H_c (Oe)	
	5K	300 K	5 K	300K	5 K	300K
125	0.039	0.018	0.007	4.194 x10^{-5}	675.380	15.620
150	0.171	0.102	0.035	3.922 x10^{-4}	545.851	14.850
200	0.004	0.002	0.001	1.484 x10^{-5}	397.462	9.520
250	0.012	0.009	0.006	6.886 x10^{-4}	363.501	11.480

Magnetic Properties

In the previous section, the effect of the annealing temperature on the formation of distinct crystalline phases of iron oxide was investigated.

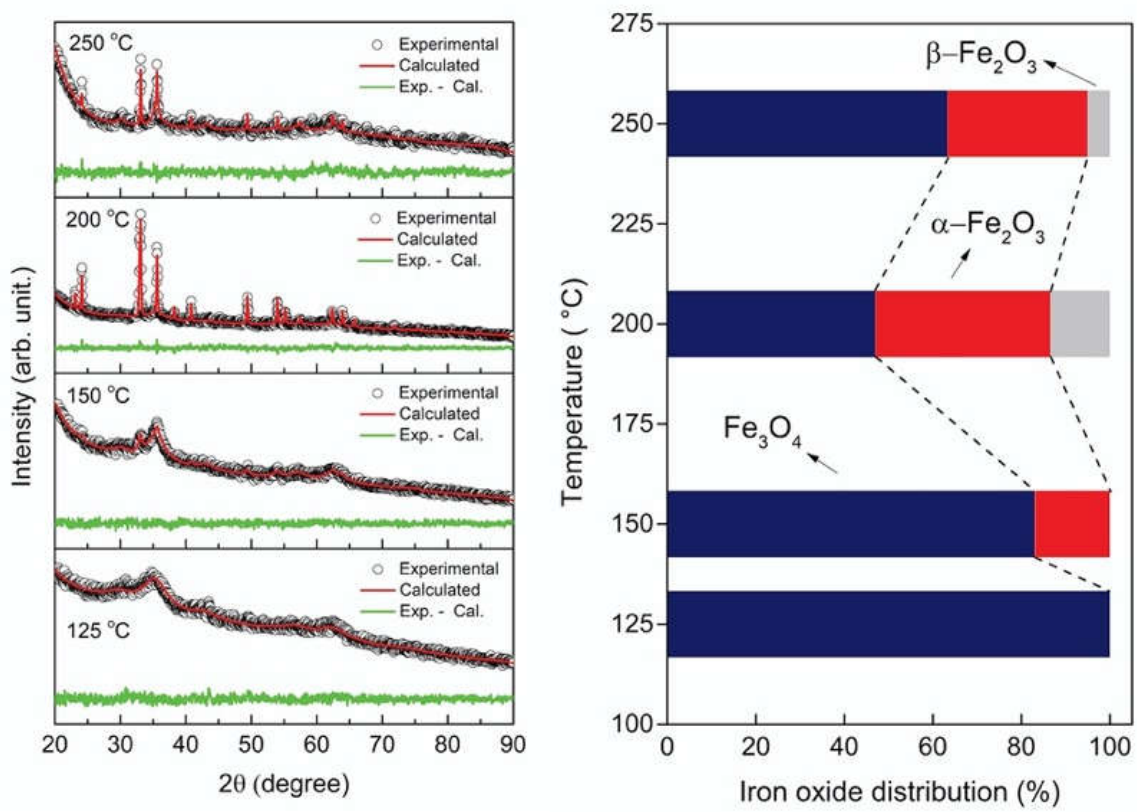

Fig. 1. (a). XRPD patterns and Rietveld refinement for the iron oxide nanoparticles oxidized at different temperatures and (b) composition of the iron oxide nanoparticles oxidized at different temperatures

The magnetic properties of nanomaterials depend on their crystal structure and average particle size. Hence, in order to investigate the effect of the iron oxide distribution on the magnetic behavior of the ferrite nanoparticles, their magnetization profiles (in terms of the magnetic field and annealing temperature) were obtained. Figure 3 (a-d) show the hysteresis curves for the nanoparticles at 5 and 300 K. As expected, at 5 K, the samples showed higher magnetic saturation than at 300 K (Table 2). This behavior is characteristic of ferrimagnetic materials (Cai, 2007). At 300 K, the samples exhibited a superparamagnetic behavior because of the formation of very short magnetic domains (Gavilán, 2017). To determine the veracity of the superparamagnetic state of the nanoparticles, a mathematical adjustment of the hysteresis curve was carried out using the Langevin function assuming a set of polydisperse nanoparticles each with a magnetic moment (μ) described by Eq. 2:

$$M(H) = n \int_0^{\infty} \mu L\left[\frac{\mu\,(\mathrm{H}-\mathrm{Hc})}{k_B T}\right] f(\mu) d\mu \qquad (2)$$

where H_C is the coercive field, n is the number of super paramagnetic particles per mass unit, K_B is the Boltzmann constant, $L(x)$ is the Langevin function, T is the absolute temperature, and $f(\mu)$ is the distribution of magnetic moments (expressed as a lognormal function: $f(\mu) = \frac{1}{\sqrt{2\pi}\,\mu\sigma} exp\left[-\frac{ln(\frac{\mu}{x_0})}{2\sigma^2}\right]$, where σis the standard deviation, $x_0$is the distribution median, and $< \mu > = x_0 exp\frac{\sigma^2}{2}$ is the mean magnetic moment. The magnetization curves of the samples and their best fitted results (solid lines in red) are shown in Fig. 4 (a-b).

From the hysteresis curves, it can be observed that at 300 K, all the samples exhibited superparamagnetism, as indicated by their very low coercivity values, unlike the case at 5 K. By Langevin adjustment, we determined the polydispersity (σ) and distribution of the mean magnetic moment <μ> of the samples, as shown in Table 3. From Table 3, it can be observed that a decrease in the annealing temperature resulted in an increase in the number of particles per unit volume (N), indicating the existence of a higher number of nanoparticles in the superparamagnetic state.

Table 3. Best fitted parameters for the M vs. H curves of the iron oxide samples at T=300 K, where n is the number of nanoparticles per unit volume, <μ> is the mean magnetic and σ is the standard deviation of the lognormal magnetic moment distribution

Annealing temperature (°C)	N (cm^{-3})	<μ> (x10^{-3} μ_B)	σ
125	1.2 x10^{17}	0.9	0.41
150	6.9 x10^{16}	1.5	0.92
200	7.6 x10^{16}	1.7	1.07
250	3.9 x10^{15}	26.9	0.92

The mean magnetic moment on the other hand increased with an increase in the annealing temperature (Fig.4c). The sample oxidized at 250 °C showed the maximum mean magnetic moment, indicating a restriction of the crystal lattices in the superparamagnetic state. The standard deviation of the lognormal magnetic moment distribution was proportional to the annealing temperature. Low values of the lognormal magnetic moment distribution confirmed the presence of nanoparticles in the superparamagnetic regime (Félix, 2017). The ZFC and FC curves of the samples oxidized at various temperatures were also obtained. Figure 5 shows that all the samples crystallized as superparamagnetic particles with grain

sizes within the single domain limit. However, the sample oxidized at 250 °C showed a flat FC curve towards higher temperatures, suggesting that this polyphase system was formed by interacting, not percolated, magnetic nanoparticles.

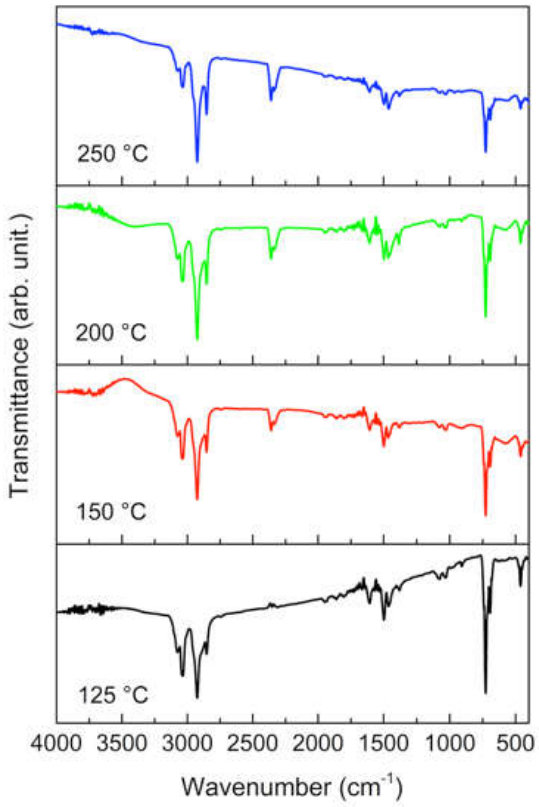

Fig. 2. FTIR spectra of the iron oxide nanoparticles oxidized at different oxidation temperatures

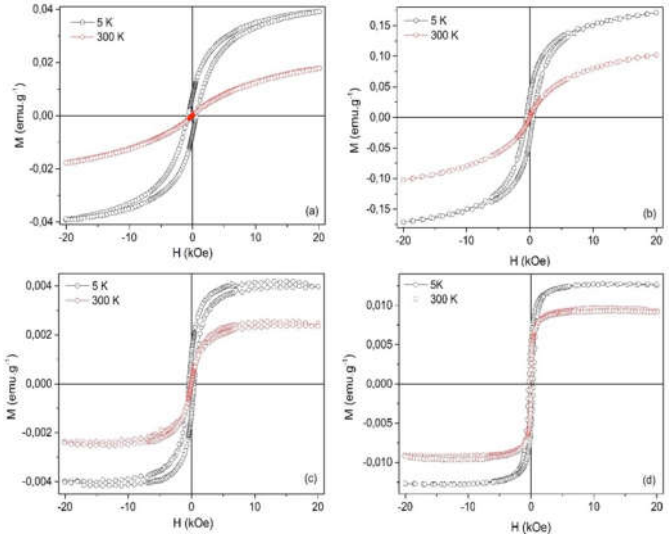

Fig. 3. Hysteresis curves for the iron oxide nanoparticles oxidized at (a) 125, (b) 150, (c) 200, and (d) 250 °C.

In this case, the blocking temperatures for the oxide systems were: 25 K (125 °C), 39 K (150 °C), 53 K (200 °C), and 150 K (250 °C). Furthermore, no Verwey transition (T_V) was detected in the case of magnetite (~120 K) because of its small diameter (Lee, 2015). Assuming that only the samples annealed at 125, 150, and 200 °C were typically superparamagnetic materials, its theoretical ZFC-FC curves were obtained according the superparamagnetic model described by Knobel *et al*. (2008).

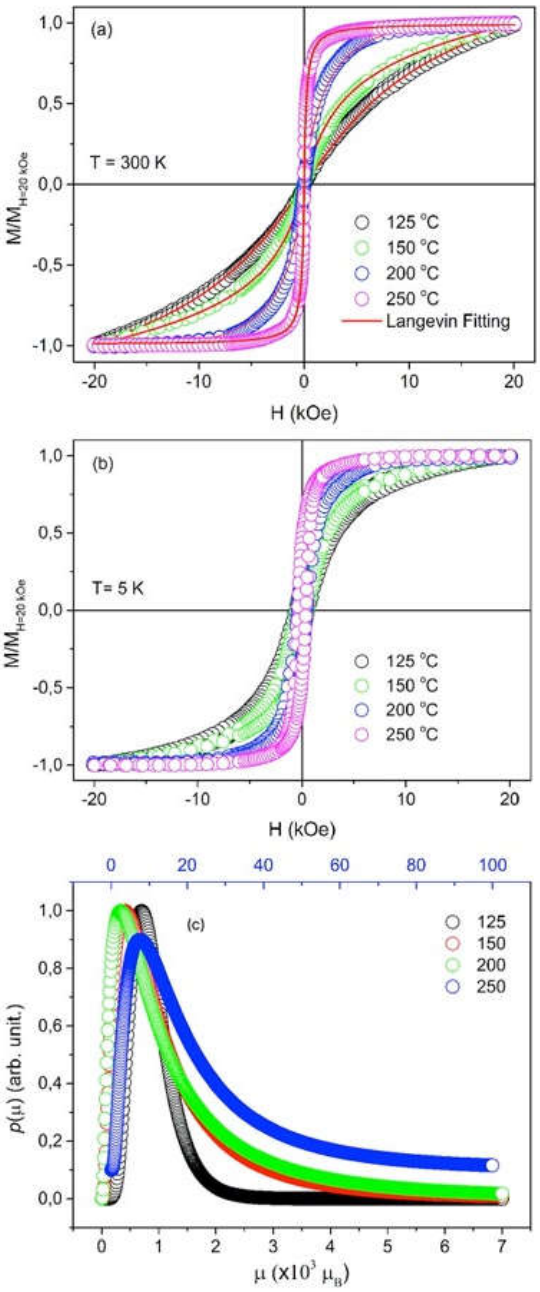

Fig. 4. Normalized magnetization curves at (a) T = 300 K, (b) T = 5 K for the samples oxidized at 125, 150, 200, and 250 °C, and (c)Log-normal distribution of the magnetic moments of the samples oxidized at 125 °C (black circles), 150°C (red circles), 200 °C (green circles) with abscissa scale of 0.0–7.5 x10^3 μ_B, and 250 °C (blue circles) with abscissa scale of 0.0 –110 x10^3 μ_B

Therefore, the initial susceptibility (assuming H is much smaller than the anisotropy field) for a single particle in the super paramagnetic regime is given by: $X_{SPM} = \mu_0 M_S^2 V / 3k_B T$ for T>T_{Ba}, where μ_0 is the vacuum permeability. On the other hand, in the clocked regime, the initial susceptibility is described as: $X_{BL} = \mu_0 M_S^2 / 3k_{eff}$ for T<T_B. The magnetic ZFC susceptibility of a system of polydisperse magnetic nanoparticles with a distribution of reduced energy barriers f(y) where $y = (E_B / E_{BM})$ and E_{BM} is the median energy barrier, is given by Eq. 3:

$$\frac{M_{ZFC}}{H} = \frac{\mu_0 M_S^2}{3k_{eff}} \left[\frac{E_{BM}}{k_B} \int_0^{T/T_{BM}} T^{-1}\, y f(y) dy + \int_{T/T_{BM}}^{\infty} f(y) dy \right] \quad (3)$$

where $T_{BM} = \frac{E_{BM}}{k_B} \ln(\tau_m / \tau_0)$, k_B is the Boltzmann constant, τ_m is the measurement time (assumed as 100 s), and τ_0 is the relaxation time.

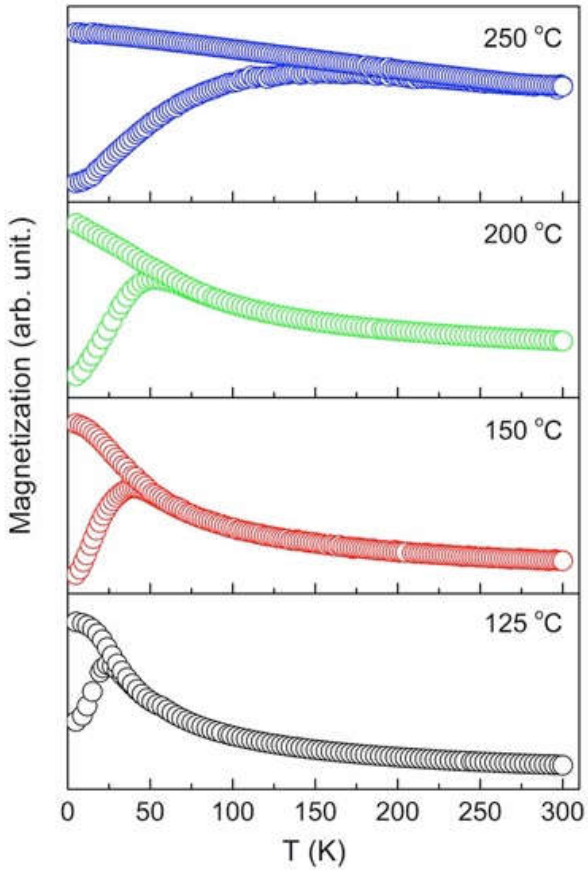

Fig. 5. ZFC and FC curves for the iron oxide nanoparticles oxidized at different temperatures

The first term in Eq. (3) corresponds to the contribution of superparamagnetic nanoparticles, while the second corresponds to the contribution from blocked magnetic nanoparticles. For FC curves, it is assumed that the contribution from blocked magnetic nanoparticles to magnetization (below T_B) is not randomly oriented. The FC susceptibility (*MFC/H*) is described by Eq. 4:

$$\frac{M_{ZFC}}{H} = \frac{\mu_0 M_S^2}{3k_{eff}} \frac{E_{BM}}{k_B} \left[\int_0^{T/T_{BM}} T^{-1}\, yf(y)dy + \int_{T/T_{BM}}^{\infty} T_B(yE_{BM}) f(y)dy \right] \quad (4)$$

The first term in Eq. (4) is contributed by superparamagnetic nanoparticles, while the second is contributed by blocked magnetic nanoparticles. We considered *f(y)* as a lognormal distribution defined as $f(y) = \frac{N}{\sqrt{2\pi} y\sigma} \exp\left(-ln^2 \frac{y}{2\sigma^2}\right)$ where σ is the standard deviation.

Figure 6 shows the best-fitted ZFC-FC curves (as red lines), and the best-fitted parameters are summarized in Table 3. Thus, it can be observed that the samples oxidized at 125 and 150 °C exhibited superparamagnetic properties because of the contribution from both the blocked and unblocked nanoparticles. However, the remaining samples showed a different magnetic regime probably because of the presence of β-Fe_2O_3.

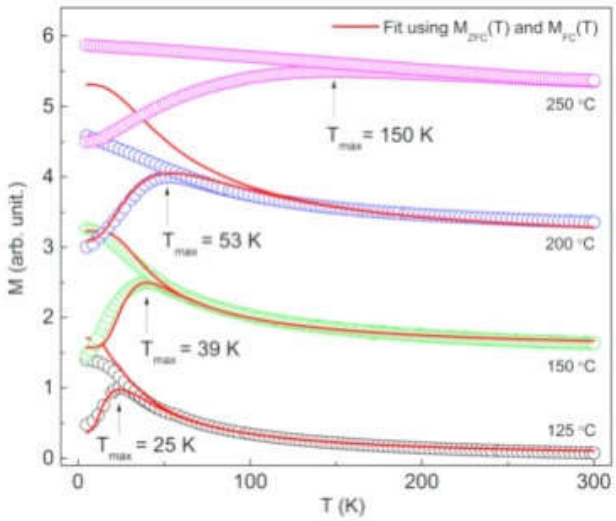

Fig. 6. ZFC-FC measurements of all the samples under a magnetic field of 50 Oe. The ZFC-FC experimental data (symbols) and fitting curves (full red line)

Table 4. Best fitted parameters obtained from the ZFC-FC experimental curves of the samples oxidized at 125, 150, and 200 °C

Annealing temperature (°C)	E_{BM} (erg)	K_{eff} (erg.cm^{-3})	τ_0 (s)	σ
125	5.60 x10^{-14}	1.06 x10^{5}	5.09 x 0^{-11}	0.55
150	8.60 x10^{-14}	9.50 x10^{4}	8.90 x10^{-9}	0.33
200	1.10 x10^{-13}	9.40 x10^{4}	1.50 x10^{-9}	0.54
250	-	-	-	-

Table 4 summarizes the magnetic parameters of the samples obtained from their fitted ZFC-FC curves. As show in Table 4, the median energy barrier (E_{BM}) decreased proportionally with the annealing temperature because of the scrambling and oscillations of the magnetic moments (Abenojar, 2016). On the other hand, the effective magnetic anisotropy (K_{eff}) of the samples increased with a decrease in the annealing temperature because of the decrease in the average particle sizes (Table 1). The relaxation time (τ_0) is an important parameter for predicting the states of thermal fluctuation associated with the energy barrier (Correia, 2014). In this study, only the sample annealed at 125 °C showed a relaxation time in the range of 10^{-10}–10^{-12}s, indicating that it existed in a superparamagnetic state.

Conclusions

Iron oxide nanoparticles were obtained using the thermal decomposition method by varying the annealing temperature. The XRD results showed that iron oxide polymorphism is widely influenced by the annealing temperature, in which either magnetite, hematiteor β-Fe_2O_3 are generated. The vibrational spectroscopy spectra showed that both the oleylamine and oleic ligands were chemisorbed on the surface of the oxide nanoparticles. The iron oxide nanoparticles annealed at low temperatures exhibit superparamagnetic behavior whereas the sample annealed at 250 °C shows a limitation of such magnetic regime.

Acknowledgments

The authorsthankthe CAPES (Coordenação de Aperfeiçoamento de Pessoal de Nível Superior). CNPq (Conselho Nacional de Desenvolvimento Científico e

Tecnológico) and FAPEMA (Fundação de Amparo à Pesquisa do Estado do Maranhão) for the financial support.

REFERENCES

Abenojar, E.C., Wickramasinghe, S., Bas-Concepcion, J., Samia, A.C.S. 2016. Structural effects on the magnetic hyperthermia properties of iron oxide nanoparticles. *Prog Nat Mater Int*. 26: 440:448. doi: 10.1016/j.pnsc. 2016.09.004.

Aliramaji, S., Zamanian, A., Sohrabijam, Z. 2015. Characterization and Synthesis of Magnetite Nanoparticles by Innovative Sonochemical Method. *Procedia Mater Sci.*11:265-269. doi: 10.1016/ j.mspro.2015.11.022.

Anjum, S., Tufail, R., Rashid, K., Zia, R., Riaz, S. 2017. Effect of cobalt doping on crystallinity, stability, magnetic and optical properties of magnetic iron oxide nano-particles. *J Magn Magn Mater.* 432:198-207. doi: 10.1016/ j.jmmm.2017.02.006.

Brázda, P., Kohout, J., Bezdička, P., Kmječ, T. 2014. α-Fe_2O_3 versus β-Fe_2O_3: Controlling the phase of the transformation product of ε-Fe_2O_3 in the Fe_2O_3/SiO_2 system. Cryst Growth. 14: 1039-1046. doi: 10.1021/ cg4015114.

Cai, W., Wan, J. 2007. Facile synthesis of superparamagnetic magnetite nanoparticles in liquid polyols. *J Colloid Interface Sci.* 305:366-370. doi: 10.1016/ j.jcis.2006.10.023.

Correia, M.J., Figueiredo, W., SChwarzacher, W. 2014. Energy barrier distributions for magnetic nanoparticles with competing cubic and uniaxial anisotropies. *Phys Lett.* A. 378:3366-3371. doi: 10.1016/j.physleta.2014.09.028.

Danno, T., Nakatsuka, D., Kusano, Y., Asaoka, H., Nakanishi, M., Fujii, T., Ikeda, Y., Takada, J. 2013. Crystal structure of β-Fe_2O_3 and topotactic phase transformation to α-Fe_2O_3. *Cryst Growth Des*.13:770-774.

Darwish, MSA. 2017. Effect of carriers on heating efficiency of oleic acid-stabilized magnetite nanoparticles. *J Mol Liq*. 231:80-85. doi: 10.1016/j.molliq.2017.01.094.

Emery, J.D., Schlepütz, C.M., Guo, P., Riha, S.C., Chang, R.P.H., Martinson, A.B.F. 2014. Atomic layer deposition of metastable β-Fe_2O_3 via isomorphic epitaxy for photoassisted water oxidation. *ACS Appl Mater Interfaces.* 6:21894−21900. doi: 10.1021/am507065y.

Félix, L.L., Coaquira, J.A.H., Martínez, M.A.R., Goya, G.F., Mantilla, J., Sousa, M.H., Valladares, L.S., Barnes, C.H.W., Morais, P.C. 2017. Structural and magnetic properties of core-shell Au/Fe_3O_4 nanoparticles. *Sci Rep.* 7:41732. doi: 10.1038/srep41732.

Fock, J., Bogart, L.K., Alonso, D.G., Espeso, J.I., Hansen, M.F., Varón, M., Frandsen, C., Pankhurst, Q.A. 2017. On the 'centre of gravity' method for measuring the composition of magnetite/maghemite mixtures, or the stoichiometry of magnetite-maghemite solid solutions, via ^{57}Fe Mössbauer spectroscopy. *J Phys D: Appl Phys*. 50:265005. doi: 10.1088/1361-6463/aa73fa.

Gaspar, A.S., Wagner, F.E., Amaral, V.S., Lima, S.A., Lhomchenko, V.A., Santos, J.G., Costa, B.F.O., Durães, L. 2017. Development of a biocompatible magnetic nanofluid by incorporating SPIONs in Amazonian oils. *Spectrochim Acta A BiomolSpectros.*172:135-146. doi: 10.1016/j.saa.2016.04.022.

Gavilán, H., Posth, O., Bogart, L.K., Steinhoff, U., Gutiérrez, L., Morales, M.P. 2017. How shape and internal structure affect the magnetic properties of anisometric magnetite nanoparticles. *Acta Mater.,* 125:416-424. doi: 10.1016/ j.actamat.2016.12.016.

Harris, R.A., Shumbula, P.M., van der, Walt, H. 2015. Analysis of the interaction of surfactants oleic acid and oleylamine with iron oxide nanoparticles through molecular mechanics modeling. Langmuir. 31:3934-3943. doi: 10.1021/acs.langmuir.5b00671.

Ianoș, R., Moacă, E.A., Căpraru, A., Lazău, R., Păcurariu, C. 2018. Maghemite, γ-Fe_2O_3, nanoparticles preparation via carbon-templated solution combustion synthesis. *Ceram Int.* 44:14090-14094. doi: 10.1016/j.ceramint. 2018.04.258.

Jin, Z., Li, Z., Pu, X., Zhao, Z., Ding, K. 2018. The mechanism for the Half-Metal to insulator transition at the $Fe_3O_4/ZnAl_2O_4$ interface. *Phys Status Solidi B.* Volume 256:1800491. doi: 10.1002/pssb.201800491.

Kamali, S., Shahmiri, N., Garitaonandia, J.S., Ångström, J., Sahlberg, M., Ericson, T., Häggström, L. 2013. Effect of mixing tool on magnetic properties of hematite nanoparticles prepared by sol–gel method. *Thin Solid Films.* 534:260-264. doi: 10.1016/j.tsf.2013.03.009.

Knobel, M., Nunes, W.C., Socolovsky, L.M., de Biasi, E., Vargas, J.M., Denardin, J.C. 2008. Superparamagnetism and other magnetic features in granular materials: a review on ideal and real systems. *J. Nanosci. Nanotechnol.* 8:2836-2857. doi: 10.1166/jnn.2008.15348.

Kohout, J., Brázda, Závěta K, Kubániová D, Kmječ T, Klementová L, Šantavá E, Lančok A. 2015. The magnetic transition in ε-Fe_2O_3 nanoparticles: Magnetic properties and hyperfine interactions from Mössbauer spectroscopy. *J Appl Phys.* 117:17D505-1-17D505-5. doi: 10.1063/ 1.4907610.

Lee, J., Kwon, S.G., Park, J.G., Hyeon, T. 2015. Size dependence of metal–insulator transition in stoichiometric Fe_3O_4 nanocrystals, Nano Lett. 15:4337-4342. doi: 10.1021/acs.nanolett.5b00331.

Lobato, N.C.C., Mansur, M.B., Ferreira, M.B. 2017. Characterization and Chemical Stability of Hydrophilic and Hydrophobic Magnetic Nanoparticles. *Mater Res.* 20:736-746. doi: 10.1590/1980-5373-MR-2016-0707.

Ma, J., Chen, K. 2018. Origin of unusual thermomagnetic behaviors in maghemite. *J Phys Chem Solids.* 112:88-93. doi: 10.1016/j.jpcs.2017.09.006.

Maccato, C., Carrato, G., Peddis, D., Varvaro, G., Barreca, D. 2018. Magnetic properties of ε iron (III) oxide nanorod arrays functionalized with gold and copper (II) oxide. Appl Surf Sci.427:890-896. doi: 10.1016/j.apsusc.2017.09.015.

Machala, L., Tuřek, J., Zbořil, R. 2011. Polymorphous transformations of nanometric iron (III) oxide: a review. Chem Mater. 23: 3255-3272. doi: 10.1021/cm200397g.

Malina, O., Kaslik, J., Tucek, J., Cuda, J., Medrik, I., Zboril, R. 2014. Thermally-Induced solid state transformation of β-Fe_2O_3 nanoparticles in various atmospheres. *AIP Conf Proc.* 1622: 89-96.doi:10.1021/cg301493a.

Malina, O., Tuček, J., Jakubec, P., Kašlik, J., Medřik, I., Tokoro, H., Yoshikiyo, M., Namai, A., Ohkoshi, S.I., Zbořil, R. 2015. Magnetic ground state of nanosized β-Fe_2O_3 and its remarkable electronic features. RSC Adv.5:49719-49727. doi: 10.1039/c5ra07484c.

Meng, Q., Wang, Z., Chai, X., Weng, Z., Ding, R., Dong, L. 2016. Fabrication of hematite (α-Fe_2O_3) nanoparticles using electrochemical deposition. *Appl Surf Sci.* 368:303-308. doi: 10.1016/j.apsusc.2016.02.007.

Mondini, S., Drago, C., Ferretti, A.M., Puglisi, A., Ponti, A. 2013. Colloidal stability of iron oxide nanocrystals coated with a PEG-based tetra-catechol *surfactant. Nanotechnology.* 24:1-14. doi:10.1088/0957-4484/24/10/105702.

Navrotsky, A. 2004. Energetic clues to pathways to biomineralization: Precursors, clusters, and nanoparticles. *Proc Natl Acad Sci.* 101:12096-12101. doi: 10.1073/pnas.0404778101.

Nigam, S., Dhirendr, B. 2017. Dendrimer-conjugated iron oxide nanoparticles as stimuli-responsive drug carriers for thermally-activated chemotherapy of cancer. Colloids Surf. B. 155:182-192. doi: 10.1016/ j.colsurfb.2017.04.025.

Sánchez, J.L., Noval, A.M., Castellano, C., Serrano, A., del Campo, A., Cabero, Varela, M., Albuín, M., de laFiguera, Maro, J.F., Astro, G.R., de la Fuente, O.R., Carmona, N. 2017. Origin of the magnetic transition at 100 K in ε-Fe_2O_3 nanoparticles studied by X-ray absorption fine structure spectroscopy. *Phys Condens Matter*. 29:485701. doi: 10.1088/1361-648X/aa904b.

Sarveena, Muraca, D., Zélis, P.M., Javed, Y., Ahmad, N., Vargas, J.M., Londoño, O.M., Knobel, M., Singh, M., Sharma, S.K. 2016. Surface and interface interplay on the oxidizing temperature of iron oxide and Au–iron oxide core–shell nanoparticles. *RSC Adv.* 6:70394-70404. doi: 10.1039/c6ra15610j.

Soares, P.I.P., Laia, C.A.T., Carvalho, A., Pereira, L.C.J., Coutinho, J.T., Ferreira, I.M.M., Novo, C.M.M., Borges, J.P. 2016. Iron oxide nanoparticles stabilized with a bilayer of oleic acid for magnetic hyperthermia and MRI applications. *Appl. Surf. Sci.* 383:240-247. doi: 10.1016/ j.apsusc.2016.04.181.

Tadic, M., Panjan, M., Damnjanovic, V., Milisevic, I. 2014. Magnetic properties of hematite (α-Fe_2O_3) nanoparticles prepared by hydrothermal synthesis method. *Appl Surf Sci.* 320:183-187. doi: 10.1016/j.apsusc.2014.08.193.

Tamirat, A.G., Rick, J., Dubale, A.A., Sun, W.N., Hwang, B.J. 2016. Using hematite for photoelectrochemical water splitting: a review of current progress and challenges. *Nanoscale Horiz.* 1:243-267. doi:10.1039/c5nh00098j.

Tuček, J., Machala, L., Ono, S., Namai, A., Yoshikiyo, M., Imoto, K., Tokoro, H., Ohkoshi, S., Zbořil, R. 2015. Zeta-Fe_2O_3–A new stable polymorph in iron (III) oxide family. *Sci Rep.* 5:1-11. doi: 10.1038/srep15091.

Vasylkiv, O., Bezdorozhev, O., Sakka, Y. 2016. Synthesis of iron oxide nanoparticles with different morphologies by precipitation method with and without chitosan addition. *J Ceram Soc Jpn.* 124:489-494. doi: 10.2109/jcersj2.15288.

Vuong, T.K., Tran, D.L., Le, T.L., Pham, D.V., Pham, H.N., Ngo, T.H.L., Do, H.M., Nguyen, X.P. 2015. Synthesis of high-magnetization and monodisperse Fe_3O_4 nanoparticles via thermal decomposition. *Mater Chem Phys.* 163:537-544. doi: 10.1016/j.matchemphys.2015.08.010.

Williams, G.V.M., Prakash, T., Kennedy, J., Chong, S.V., Rubanov, S. 2018. Spin-dependent tunneling in magnetite nanoparticles. *J MagnMagn Mater.* 460:229-233. doi: 10.1016/j.jmmm.2018.04.017.

Wu, W., Chang, Z.J., Vellaisamy, A.L.R. 2016. Designed synthesis and surface engineering strategies of magnetic iron oxide nanoparticles for biomedical applications. Nanoscale.8:19421-19474.doi: 10.1039/c6nr07542h.

Wu, W., Z. Wu, T. Yu, C. J, Woo-Sik K. 2015. Recent progress on magnetic iron oxide nanoparticles: synthesis, surface functional strategies and biomedical applications. *Sci Technol Adv Mater.* 16:023501. doi: 10.1088/1468-6996/16/2/023501.

Xu, K., Feng, J.S., Liu, Z.P., Xiang, H.J. 2018. Origin of Ferrimagnetism and Ferroelectricity in Room-Temperature Multiferroic ε-Fe_2O_3. *Phys Rev Appl.* 9:044011-1-044011-7. doi: 10.1103/ *Phys Rev Applied.* 9.044011.

Yakushkin, S.S., Balaev, D.A., Dubrovskiy, A.A., Semenov, S.V., Knyazev, Y.V., Bayukov, O.A., Kirillov, V.L., Ivantsov, R.D., Edelman, I.S., Martyanov, O.N. 2018. ε-Fe_2O_3 Nanoparticles Embedded in Silica Xerogel–Magnetic Metamaterial. *Ceram Int.* 44:17852-17857.doi: 10.1016/j.ceramint.2018.06.254.

Zboril, R., Mahala, L., Mashlav, M., Sharma, V. 2004. Iron (III) oxide nanoparticles in the thermally induced oxidative decomposition of Prussian blue, $Fe_4[Fe(CN)_6]_3$. *Cryst Growth Des.* 4:1317-1325. doi: 10.1021/cg049748+.

****